

Imprinting of skyrmions and bimerons in an antiferromagnet

Coline Thevenard,^{1,*} Miina Leiviskä,¹ Richard F. L. Evans,^{2,†} Daria Gusakova,¹ Vincent Baltz^{1,‡}

¹*Univ. Grenoble Alpes, CNRS, CEA, Grenoble INP, IRIG-SPINTEC, F-38000 Grenoble, France*

²*School of Physics, Engineering and Technology, University of York, York YO10 5DD, United Kingdom*

**coline.thevenard@cea.fr; †richard.evans@york.ac.uk; ‡vincent.baltz@cea.fr*

Abstract

Topologically protected magnetic states in condensed matter physics, particularly antiferromagnetic (AFM) skyrmions (Sks) and bimerons (Bms), offer promising prospects for terahertz dynamics and sustained current-induced motion, thanks to their compensating multiple sub-lattice structure. However, nucleating AFM Sks and Bms is challenging due to the lack of net magnetization. Previous attempts to imprint pre-defined Sks and Bms in a ferromagnet (FM) and transfer them to an AFM using interfacial exchange bias in FM/AFM heterostructures have been hindered by complex multilayers with discontinuities, polycrystallinity, or multipartite chiral AFMs. Employing atomistic spin simulations, we demonstrate the viability of texture imprinting for nucleating Sks and Bms in AFMs, using a prototypical bipartite AFM layer in a multilayer structure free from discontinuities. Such imprinting is a crucial step towards understanding the static and dynamic properties of natural antiferromagnetic textures and their unique properties.

I. Introduction

The interest in topologically protected states in condensed matter physics stems from their robustness against small perturbations and their significant impact on the physical properties of the system. This impact is closely tied to the system's symmetry, which for example enables a non-zero geometric phase for electrons interacting with the spin structure. While topological objects in uncompensated magnets, like ferromagnets (FMs), have been extensively studied due to their fundamental significance and potential applications [1,2], the presence of multiple spin sub-lattices in compensated magnets with zero net magnetization, like antiferromagnets (AFMs) and altermagnets opens new avenues for topological phenomena and spintronic applications [3–8]. Specifically, real-space topological states, such as AFM skyrmions (Sks) and bimerons (Bms) - in-plane topological homeomorphic counterparts of Sks - exhibit intriguing properties. Due to anti-parallel interatomic exchange interactions, AFM Sks and Bms possess zero net magnetization and topological charge, ensuring robustness against external fields and vanishing net topological charge and Hall effects [9–11]. Moreover, they are predicted to induce unique transport properties, including a non-vanishing topological spin Hall effect [12,13] and a longitudinal Sk velocity unconstrained by the Sk Hall effect, exceeding that of FM Sks due to the inherent THz dynamics in AFMs [14,15]. These properties make AFM Sks and Bms not only fascinating subjects for studies on topology but also promising candidates for ultra-dense, ultra-fast, low-power spintronic devices. However, the main challenge in accessing these advantageous properties is the difficulty in experimentally nucleating AFM Sks and Bms due to the lack of net magnetization. Various nucleation techniques have been proposed, including field-assisted methods, magneto-electric effects and ultrafast laser pulses [7]. An alternative approach involves pre-defining Sks and Bms in a FM and subsequently imprinting them in the AFM using interfacial exchange bias in FM/AFM heterostructures, facilitated by appropriate thermal and magnetic field cycles. This method has successfully transferred spin textures in AFMs, such as vortices, domain walls and non-topologically protected bubbles [7,16–20]. For Sks and Bms, both simulations and experiments have attempted to validate this imprinting method, but complex multilayers with discontinuities, polycrystallinity, or multipartite chiral AFMs have hindered accurate calculations of topological parameters [7,19,20]. In this study, we employ atomistic simulations to demonstrate the viability of texture imprinting for nucleating Sks and Bms in AFMs. Using a prototypical bipartite AFM layer in a multilayer structure free from discontinuities, we quantitatively confirm the imprinting of actual Sks and Bms in an AFM, starting from pre-defined FM Sks and Bms [Fig. 1].

II. Atomistic simulation system

The numerical study focuses on a single-crystal AFM (n)/NM (1)/FM (3)/HM (1 ML) system [Fig. 1(a)], where the number of monolayers (MLs) is indicated in parenthesis, with n ranging from 11 to 28 MLs.

The crystal structure is consistently set to that of two interpenetrating single cubic lattices and equivalent to rocksalt, with a lattice parameter of 4.17 Å. The area of the simulation system is 100×100 nm². The crystal is oriented along the [001] direction, taken as the z-axis and features a continuous structure. Periodic boundary conditions are applied in the x ([100] direction) and y ([010] direction), to simulate an infinite system. The roles of the non-magnetic (NM) layer in inducing magnetic frustration for exchange bias coupling and the heavy metal (HM) layer in promoting perpendicular anisotropy and spin canting to stimulate spin textures formation [18,19] will be detailed later in the text.

Simulations are performed using the VAMPIRE atomistic simulation software [21] on the ARCHER2 supercomputer, each utilizing 1024 processors across 8 physical nodes. The large-scale simulation involves 10⁶ time steps and employs the adaptative Monte Carlo algorithm to minimize the energy of up to 7.6×10⁶ spins [22].

The interactions within the system are governed by the spin Hamiltonian [23]

$$\mathcal{H} = - \sum_{i < j} J_{ij} (\mathbf{S}_i \cdot \mathbf{S}_j) - \sum_{i < j} \mathbf{D}_{ij} \cdot (\mathbf{S}_i \times \mathbf{S}_j) - \sum_{i < j} \frac{k_{N,ij}}{2} (\mathbf{S}_i \cdot \mathbf{e}_{ij})^2 - \sum_i k_{u,i} (\mathbf{S}_i \cdot \mathbf{e}_i)^2 - \sum_i \mu_{s,i} \mathbf{S}_i \cdot \mathbf{B}_{\text{ext}}$$

where the indices i and j refer to the position of the atomic sites occupied by spins of vector \mathbf{S} and magnetic moment μ_s . The Heisenberg exchange interaction, parametrized by the constant J_{ij} , is represented by the first term. The second term accounts for the Dzyaloshinskii-Moriya interaction (DMI), described by the vector $\mathbf{D}_{ij} = D_{ij}(\hat{\mathbf{r}}_{ik} \times \hat{\mathbf{r}}_{jk})$, where D_{ij} is the DMI strength and $\hat{\mathbf{r}}_{ik,jk}$ the unit vector joining the magnetic atoms at sites i and j and the non-magnetic atom at site k . The third term introduces a radial spin rotation with respect to a specific nearest neighbor, inducing interface perpendicular anisotropy and relating to the Néel surface anisotropy characterized by the constant $k_{N,ij}$. The fourth term introduces a uniaxial anisotropy of constant $k_{u,i}$, along the axis of unit vector \mathbf{e}_i and the last term is the Zeeman interaction, which couples the spins to an external induction \mathbf{B}_{ext} .

The magnetic properties of the HM/FM bilayer are based on those of Pt/Co which have been optimized to nucleate Sk in the FM [18,24]. Specifically, the interfacial perpendicular magnetic anisotropy is $k_{N,\text{HM-FM}} = 2 \times 10^{-24}$ J/atom and the DMI is $D_{\text{HM-FM}} = 10^{-21}$ J/link. The FM has an atomic magnetic moment $\mu_{s,\text{FM}} = 1.37 \mu_B$, an exchange constant $J_{\text{FM}} = 13.3 \times 10^{-21}$ J/link (which corresponds to the Curie temperature $T_C = 1385$ K) and (i) a uniaxial anisotropy $k_{u,\text{FM}} = 10^{-24}$ J/atom for the Sk case [Fig. 1(b)] or (ii) a hard-axis anisotropy $k_{u,\text{FM}} = -10^{-23}$ J/atom for the Bm case [Fig. 1(c)]. In its ground state, the AFM is composed of two collinear spin sublattices, AFMa and AFMb, hosting an atomic magnetic moment $\mu_{s,\text{AFMa(b)}} = 2 \mu_B$, coupled antiparallel via a negative exchange constant $J_{\text{AFM}} = -5.04 \times 10^{-21}$ J/link (which corresponds to the Néel temperature $T_N = 525$ K), and subject to: (i) a uniaxial anisotropy along the z-axis $k_{u,\text{AFM}} = 10^{-25}$ J/atom for the Sk case [Fig. 1(b)], or (ii) a hard-axis anisotropy $k_{u,\text{AFM}}$

$= -10^{-24}$ J/atom for the Bm case [Fig. 1(c)]. The FM and the AFM are coupled via an interfacial exchange interaction $J_{\text{FM-AFM}} = 10^{-21}$ J/link. We note that conversion to SI units is provided in Table S1 in the SM. To imprint spin textures in the AFM, exchange bias coupling requires a net interfacial magnetic moment [25]. A monolayer mixed with FM and populated with 75% of substituted NM atoms creates a net interfacial magnetic moment that provides a reasonable exchange bias, while preserving a flat interface, which is essential for further calculating the topology of the imprinted textures in the AFM.

III. Imprinting of AFM spin textures

The nucleation and stabilization processes of AFM SkS are depicted in Figure 2. They require three successive simulation steps [7,16–20,24]. First, SkS are formed in the FM layer only, at 600 K under an applied field of 0.5 T along the z-axis. In this step, the FM is magnetically ordered [Fig. 2(a) and S1] while the AFM remains disordered, as 600 K is below the FM's Curie temperature $T_C = 1385$ K and above the AFM's Néel temperature $T_N = 525$ K [Fig. 2(b,c) and S1]. The effect of the field strength and DMI in favoring the formation of SkS in the FM over maze domains or full saturation is shown in Fig. S2 in the SM. Next, AFM spin textures are imprinted via exchange coupling at the FM/AFM interface. The system is cooled from 600 to 0 K, in the same applied field of 0.5 T. This thermal process leads to the collapse of one Sk and the stabilization of the other in the FM [Fig. 2(d,g)]. Upon crossing T_N , the AFM orders and interfacial coupling is triggered, setting the Sk in the AFM [Fig. 2(e,f)]. The resulting AFM texture consists of two interlocked FM SkS with opposite polarity [Fig. 2(h,i)]. We note that using 0 K avoids thermal noise, facilitating the visual identification and quantification of the spin textures' topological nature, as will be detailed later in the text. Finally, the applied field is removed to reach remanence. This step widens the FM [Fig. 2(j)] and AFM Sk's radius and wall width [Fig. 2(k,l)], as expected from the field-dependent energy landscape of FM SkS [26] [see also Fig. S1 in the SM].

IV. Tubular skyrmion

The assignment of the given topological class to the SkS is obtained by calculating their topological charge Q [Fig. 3(a)] [1,2,7]. For a two-dimensional discrete lattice of spins (i. e. for each ML in system) Q is a sum of local densities q calculated for a square cell [insert of Fig. 3(a)] [27,28]:

$$q(\mathbf{x}^*) = \frac{1}{4\pi} \sum_{(i,j,k) \in \{(1,2,3), (1,3,4)\}} 2 \tan^{-1} \left(\frac{\mathbf{s}_i \cdot (\mathbf{s}_j \times \mathbf{s}_k)}{1 + \mathbf{s}_i \cdot \mathbf{s}_j + \mathbf{s}_i \cdot \mathbf{s}_k + \mathbf{s}_j \cdot \mathbf{s}_k} \right).$$

Figure 3 demonstrates the topological nature of the nucleated SkS in the FM below 529 K, with a topological charge $Q = 2$, which reduces to 1 upon annihilation of one FM Sk at 359 K. It also demonstrates the topological nature of the imprinted Sk in the AFM below 207 K with $Q = +(-)1$ for

the AFMb (AFMa) sublattices. The values were confirmed throughout the depth of the AFM. At higher temperatures, thermal fluctuations can cause neighboring spins to deviate significantly from each other resulting in deviation of Q from an integer value [27] [Fig. 3(b-m)]. Note that the Sk imprinted in the AFM consists of two intercalated FM Sk with mutually reversed spins [Fig. 4(a)] resulting in an AFM Sk with a net topological charge of zero [29].

To investigate the intricate topology of the Sks formed with more accuracy, the usual three key parameters are introduced and calculated: polarity, vorticity and helicity [1,2,7]. Polarity p quantifies the out-of-plane magnetization density of the Sk core, vorticity m represents the magnetization density winding number, and helicity γ describes the angular phase shift between the spatial magnetization rotation and the positional winding. We note that $Q = pm$. In its final state [Fig. 2(j-l)], $(p, m, \gamma) = (1, 1, \pi)$ for the FM layer and $(-1, -1, 0)$ and $(1, 1, \pi)$ for the AFMa and AFMb sublattices of the AFM layer, respectively. These values indicate that the initial Sk in the FM is of the Néel type, consistent with the DMI strength of 10^{-21} J/link which exceeds the critical strength for a Bloch to Néel domain wall transition $D_c = 4\mu_0 M_s^2 t \ln 2 / (2\pi^2) = 10^{-23}$ J/link [30]. The Sk imprinted in the AFM sublattices naturally replicates the morphology and topology (in terms of p , m and γ) of the Sks from which it originates in the FM layer.

Due to the regularity of the atomic lattice and continuity at the interfaces, the FM (AFM) Sk in their final states [Fig. 2(j-l)] form a disc with in-plane spins describing a circle of radius $R = 7.8$ (7.1) nm and wall width $w = 8.5$ (9.7) nm, estimated by fitting $s_z(r) = \cos(2 \tan^{-1}(\sinh(r/w) \sinh(R/w)))$ [31]. The close values for both materials clearly indicate that the arrangement of the AFM spins follows that of the FM spins.

Next, we investigated how the topological texture propagates from the interface through the depth of the AFM and how temperature affects this propagation. To quantify the depth-dependent arrangement of each AFM sublattice spins relative to the FM spins, we employed the partial spin-spin correlation function [Fig. 4(b)]:

$$C(\Delta z) = \frac{1}{N} \sum_{(i,j)} s_{z,i} s_{z,j}(\Delta z)$$

where Δz is the distance to the FM/AFM interface and N is the number of spin pairs formed by the FM spin i and AFM j of the same in-plane coordinates (x,y) [19]. This quantitative method enhances the bare observation of cross-sections [Fig. 4(c)]. The sign of C is naturally opposite when considering the two AFM sublattices of opposite spins.

Starting from fully anticorrelated spins ($C \approx 0$) at 600 K, when the AFM is disordered, the system gradually reaches full correlation ($|C| \approx 1$) at 0 K, across the entire AFM layer. This indicates that the replication is effective throughout the 5.8 nm-thick AFM layer, which corresponds to the maximum

penetration depth allowed for this set of parameters (Fig. S3 in the SM). We note however that, when the correlation remains constant in the core of the AFM layer, it deteriorates in the few MLs at the FM/AFM interface due to the loss of surface exchange bonds and a local decrease in AFM surface order. Similarly, the correlation also deteriorates in the last few MLs away from the free AFM edge, due to the dominant influence of the AFM exchange. In other words, close to the edge, the decorrelation from the FM prevents the rearrangement of the AFM spins.

V. Tubular bimeron

To test the universality of the replication, we next simulate the same heterostructure under identical energetic conditions, with the sole modification being the change of anisotropy from out-of-plane to in-plane. Specifically, the FM constant $k_{u,FM} = -10^{-23}$ J/atom and the AFM constant $k_{u,AFM} = -10^{-24}$ J/atom now confine the magnetization to the xy-plane. This allows us to nucleate an in-plane Sk, or a Bm in the FM layer and to imprint it throughout the thickness of the AFM layer [Fig. 1(c) and 5], using the thermal and field procedure (Figs. S4 and S5 in the SM) described earlier in the text. In the final state, the axis of the Bm, which joins the centers of the two merons is angled by -3.3° in the xy-plane with respect to the x-axis. This in-plane orientation is a consequence of using z as the hard axis, allowing the Bm axis to lie anywhere within the isotropic xy-plane. Additionally, the axis is tilted out-of-plane by 1.5° ascribed to magnetic frustration at the FM/AFM interface, combined with the residual out-of-plane interfacial anisotropy k_N . Moreover, by analogy with a Sk, the topological parameters of the spins are $(p, m, \gamma) = (1, 1, \pi)$ for the FM layer, and $(-1, -1, 0)$ and $(1, 1, \pi)$ for the AFMa and AFMb sublattices, respectively. These parameters were calculated after applying a rotation operation to align the Bm axis with the z-axis. The invariance of the topological parameters, along with an identical topological charge $Q = 1$ for the FM layer and AFMb sublattice and -1 for the AFMa sublattice, confirms that the texture we imprinted in the AFM layer is a Bm, a quasiparticle homeomorphic to the Sk imprinted in the first part of this work [9,32].

VI. Conclusion

In conclusion, we have theoretically validated the feasibility of texture imprinting for the nucleation of actual skyrmions and bimerons in a compensated magnet with zero net magnetization, employing predefined skyrmions and bimerons in an adjacent exchange-coupled ferromagnet as a template. Our study involves engineering a prototypical bipartite antiferromagnetic layer within a multilayer structure, ensuring the presence of the necessary Dzyaloshinskii-Moriya interaction (DMI), perpendicular anisotropy, and interfacial magnetic frustrations, all while avoiding discontinuities. This approach has enabled us to calculate the topological parameters of the imprinted spin textures, providing quantitative

data that was previously inaccessible due to the complexities of multilayers with discontinuities, polycrystallinity, or multipartite chiral antiferromagnets. We have successfully tracked the formation of the topological objects throughout the thermal procedure, first nucleating skyrmions and bimerons in the ferromagnet, and then replicating them in the antiferromagnet after crossing the Néel temperature. The replicated skyrmions and bimerons were found to extend beyond the interface, spanning the core of the antiferromagnet. This work addresses the challenge of nucleating quantitatively proven topological magnetic textures in compensated magnets with zero net magnetization. It paves the way for extending the study of topological spin textures beyond ferromagnets, into materials with intriguing electrodynamic properties, such as antiferromagnets and altermagnets.

Acknowledgments

This study was partially supported by the CNRS international research project (IRP) “CITRON”, the U.K. EPSRC program (Grant No. EP/V007211/1), and the French National Research Agency through the France 2030 government grant PEPR-SPIN “ALTEROSPIN” ANR-24-EXPR-0002. This work used the ARCHER2 UK National Supercomputing Service. Derived data supporting the findings of this study are available on request.

References

- [1] A. Soumyanarayanan, N. Reyren, A. Fert, and C. Panagopoulos, Emergent phenomena induced by spin–orbit coupling at surfaces and interfaces, *Nature* **539**, 509 (2016).
- [2] B. Göbel, I. Mertig, and O. A. Tretiakov, Beyond skyrmions: Review and perspectives of alternative magnetic quasiparticles, *Phys. Rep.* **895**, 1 (2021).
- [3] T. Jungwirth, X. Marti, P. Wadley, and J. Wunderlich, Antiferromagnetic spintronics, *Nat. Nanotechnol.* **11**, 231 (2016).
- [4] V. Baltz, A. Manchon, M. Tsoi, T. Moriyama, T. Ono, and Y. Tserkovnyak, Antiferromagnetic spintronics, *Rev. Mod. Phys.* **90**, 015005 (2018).
- [5] L. Šmejkal, J. Sinova, and T. Jungwirth, Emerging Research Landscape of Altermagnetism, *Phys. Rev. X* **12**, 040501 (2022).
- [6] V. Bonbien, F. Zhuo, A. Salimath, O. Ly, A. Abbout, and A. Manchon, Topological aspects of antiferromagnets, *J. Phys. D: Appl. Phys.* **55**, 103002 (2022).
- [7] M. Leiviskä et al., Antiferromagnetic skyrmions in spintronics, Elsevier (Eds A. Hirohata Al.) (2024).
- [8] O. J. Amin et al., Antiferromagnetic half-skyrmions electrically generated and controlled at room temperature, *Nat. Nanotechnol.* **18**, 849 (2023).
- [9] B. Göbel, A. Mook, J. Henk, I. Mertig, and O. A. Tretiakov, Magnetic bimerons as skyrmion analogues in in-plane magnets, *Phys. Rev. B* **99**, 060407 (2019).
- [10] L. Shen, X. Li, J. Xia, L. Qiu, X. Zhang, O. A. Tretiakov, M. Ezawa, and Y. Zhou, Dynamics of ferromagnetic bimerons driven by spin currents and magnetic fields, *Phys. Rev. B* **102**, 104427 (2020).
- [11] L. Shen, J. Xia, X. Zhang, M. Ezawa, O. A. Tretiakov, X. Liu, G. Zhao, and Y. Zhou, Current-Induced Dynamics and Chaos of Antiferromagnetic Bimerons, *Phys. Rev. Lett.* **124**, 037202 (2020).
- [12] J. Barker and O. A. Tretiakov, Static and Dynamical Properties of Antiferromagnetic Skyrmions in the Presence of Applied Current and Temperature, *Phys. Rev. Lett.* **116**, 147203 (2016).
- [13] E. G. Tveten, A. Qaiumzadeh, O. A. Tretiakov, and A. Brataas, Staggered Dynamics in Antiferromagnets by Collective Coordinates, *Phys. Rev. Lett.* **110**, 127208 (2013).
- [14] P. M. Buhl, F. Freimuth, S. Blügel, and Y. Mokrousov, Topological spin Hall effect in antiferromagnetic skyrmions, *Phys. Status Solidi - Rapid Res. Lett.* **11**, 1700007 (2017).
- [15] C. A. Akosa, O. A. Tretiakov, G. Tatara, and A. Manchon, Theory of the Topological Spin Hall Effect in Antiferromagnetic Skyrmions: Impact on Current-Induced Motion, *Phys. Rev. Lett.* **121**, 097204 (2018).
- [16] G. Salazar-Alvarez et al., Direct evidence of imprinted vortex states in the antiferromagnet of exchange biased microdisks, *Appl. Phys. Lett.* **95**, 012510 (2009).
- [17] J. Wu et al., Direct observation of imprinted antiferromagnetic vortex states in CoO/Fe/Ag(001) discs, *Nat. Phys.* **7**, 303 (2011).
- [18] K. G. Rana et al., Imprint from ferromagnetic skyrmions in an antiferromagnet via exchange bias, *Appl. Phys. Lett.* **119**, 192407 (2021).
- [19] M. Leiviskä, S. Jenkins, R. F. L. Evans, D. Gusakova, and V. Baltz, Local setting of spin textures in a granular antiferromagnet, *Phys. Rev. B* **108**, 184424 (2023).

- [20] B. He et al., Creation of Room-Temperature Sub-100 nm Antiferromagnetic Skyrmions in an Antiferromagnet IrMn through Interfacial Exchange Coupling, *Nano Lett.* **24**, 2196 (2024).
- [21] R. F. L. Evans, W. J. Fan, P. Chureemart, T. A. Ostler, M. O. A. Ellis, and R. W. Chantrell, Atomistic spin model simulations of magnetic nanomaterials, *J. Phys. Condens. Matter* **26**, 103202 (2014).
- [22] J. D. Alzate-Cardona, D. Sabogal-Suárez, R. F. L. Evans, and E. Restrepo-Parra, Optimal phase space sampling for Monte Carlo simulations of Heisenberg spin systems, *J. Phys. Condens. Matter* **31**, 095802 (2019).
- [23] S. Jenkins, Spin Dynamics Simulations of Iridium Manganese Alloys, University of York, 2020.
- [24] S. Brück, J. Sort, V. Baltz, S. Suriñach, J. S. Muñoz, B. Dieny, M. D. Baró, and J. Nogués, Exploiting Length Scales of Exchange-Bias Systems to Fully Tailor Double-Shifted Hysteresis Loops, *Adv. Mater.* **17**, 2978 (2005).
- [25] S. Jenkins, W. J. Fan, R. Gaina, R. W. Chantrell, T. Klemmer, and R. F. L. Evans, Atomistic origin of exchange anisotropy in noncollinear γ -IrMn₃-CoFe bilayers, *Phys. Rev. B* **102**, 140404 (2020).
- [26] X. S. Wang, H. Y. Yuan, and X. R. Wang, A theory on skyrmion size, *Commun. Phys.* **1**, 31 (2018).
- [27] B. Berg and M. Lüscher, Definition and statistical distributions of a topological number in the lattice O(3) σ -model, *Nucl. Phys. B* **190**, 412 (1981).
- [28] M. Böttcher, S. Heinze, S. Egorov, J. Sinova, and B. Dupé, B-T phase diagram of Pd/Fe/Ir(111) computed with parallel tempering Monte Carlo, *New J. Phys.* **20**, 103014 (2018).
- [29] O. A. Tretiakov, D. Clarke, G. W. Chern, Y. B. Bazaliy, and O. Tchernyshyov, Dynamics of Domain Walls in Magnetic Nanostrips, *Phys. Rev. Lett.* **100**, 127204 (2008).
- [30] A. Thiaville, S. Rohart, É. Jué, V. Cros, and A. Fert, Dynamics of Dzyaloshinskii domain walls in ultrathin magnetic films, *Europhys. Lett.* **100**, 57002 (2012).
- [31] H. B. Braun, Fluctuations and instabilities of ferromagnetic domain-wall pairs in an external magnetic field, *Phys. Rev. B* **50**, 16485 (1994).
- [32] Y. Shen, Q. Zhang, P. Shi, L. Du, X. Yuan, and A. V. Zayats, Optical skyrmions and other topological quasiparticles of light, *Nat. Photonics* **18**, 15 (2024).

Figures and captions

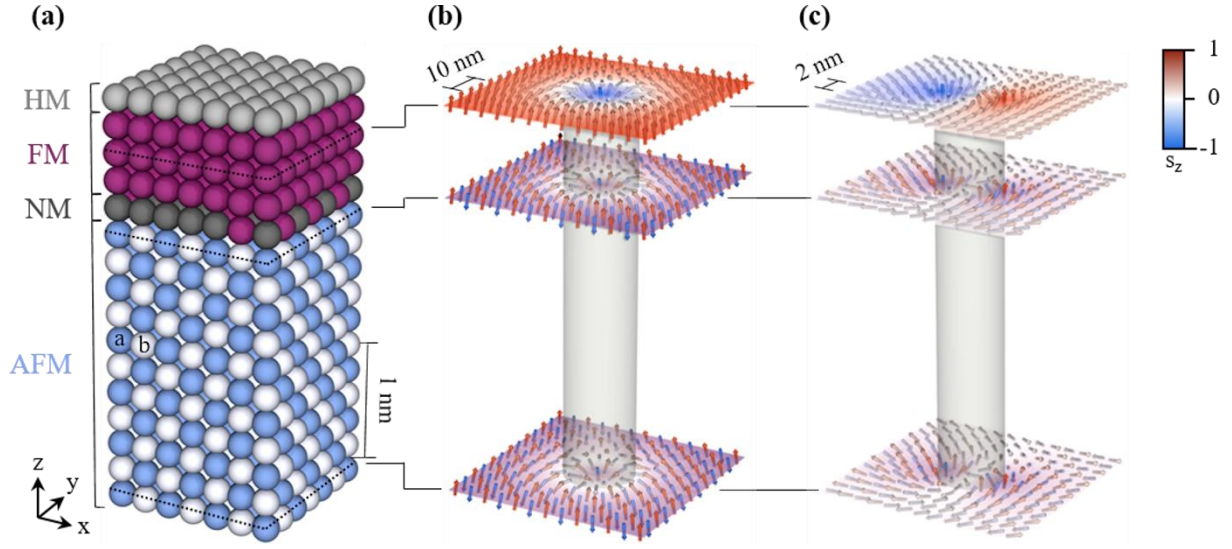


Figure 1. (a) The atomic structure of the simple cubic monocrystalline simulation system consisting of: a HM/FM bilayer for Sk nucleation, a 75%-rich NM interface for coupling, and a prototypical bipartite AFM layer made of two sublattices: AFMa and AFMb. In their ground state, the spins of AFMa and AFMb are collinear and opposite. The full size of the simulation system is $100 \times 100 \times 3.34 \text{ nm}^3$ corresponding to 1 monolayer (ML) of HM, 3 MLs of FM, 1 ML of NM and 11 MLs of AFM. 3D views of the Sk (b) and Bm (c) tubes obtained in the FM and imprinted in the 11 MLs-thick AFM, following thermal and magnetic field cycling procedures. The simulated spins oriented in the xy- (b) yz- (c) plane define the contour of the tube.

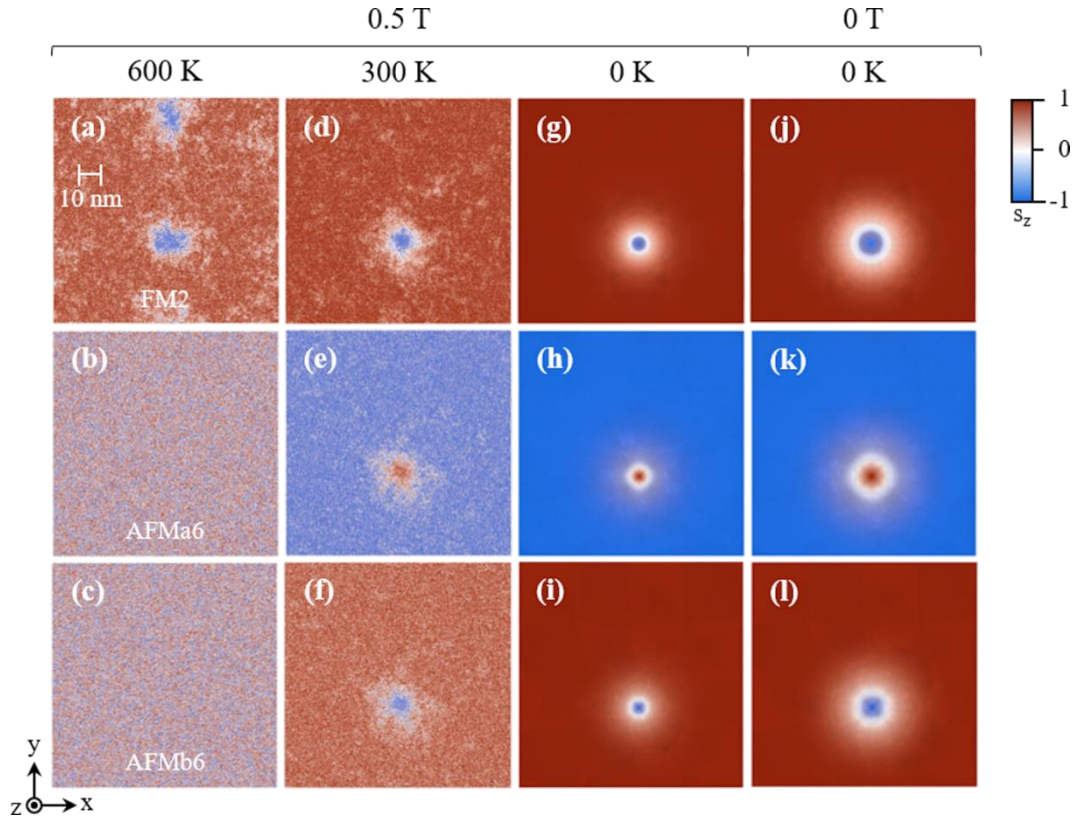


Figure 2. Top view cross section snapshots of the evolution of the spin textures in the FM (first row, 2nd ML from the FM/AFM interface), and the AFM in the core (second row: AFMa sublattice, third row: AFMb sublattice, 6th ML from the FM/AFM interface). First column: field-induced nucleation in the FM, below the Curie temperature (T_C) of the FM and above the Néel temperature (T_N) of the AFM (Fig. S1 in SM). Second and third columns: imprinting and stabilization of Sks in the AFM, via cooling across T_N . Fourth column: remanence state.

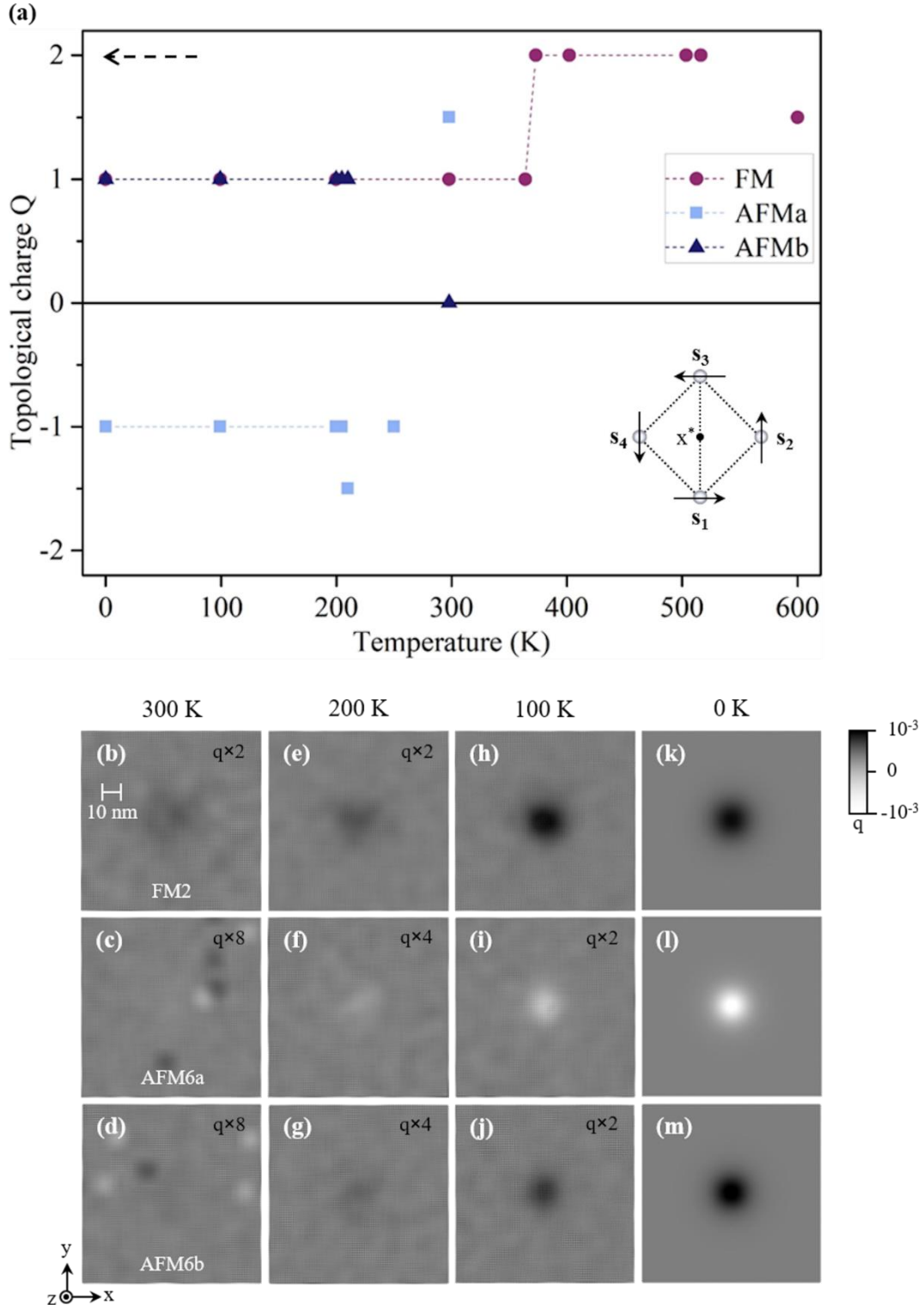


Figure 3. (a) Temperature dependence of the topological charge $Q = \sum_{x^*} q(x^*)$ for the FM and both sublattices of the AFM. The dotted arrow indicates the timeline. Insert: schematic showing the discretization method for calculating q , for a two-dimensional square cell. (b-m) Spatial distribution of the topological charge density q after post-processing the raw data images (Fig. S6 in the SM) with a Gaussian filter for better visibility (SM). Note that Q was calculated from the unprocessed q .

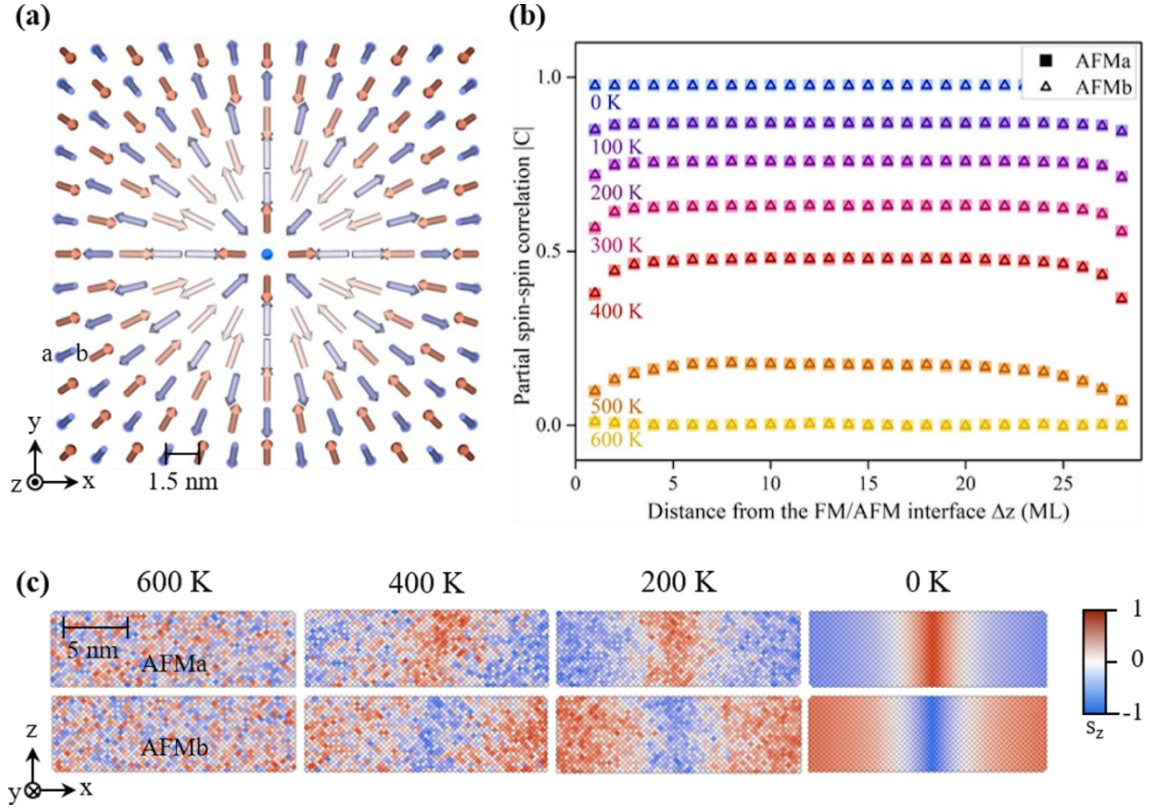


Figure 4. (a) Zoom on the top view cross section of the intertwined AFMa- and AFMb-sublattice Sk, imprinted in the 28 MLs-thick AFM (6th ML from the FM/AFM interface), at remanence, following thermal and magnetic field cycling procedures. To facilitate the reading of the image, only 1 out of every 7 spins is shown. (b) Temperature-dependence of the modulus of the sublattice-resolved partial spin-spin correlation function applied in the center of the spin texture imprinted in the AFM. (c) Side view cross section at selected temperatures, showing the formation of the Sk tube in the AFM.

Supplemental material:

Imprinting of skyrmions and bimerons in an antiferromagnet

Coline Thevenard,¹ Miina Leiviskä,¹ Richard F. L. Evans,² Daria Gusakova,¹ Vincent Baltz¹

¹Univ. Grenoble Alpes, CNRS, CEA, Grenoble INP, IRIG-SPINTEC, F-38000 Grenoble, France

²School of Physics, Engineering and Technology, University of York, York YO10 5DD, United Kingdom

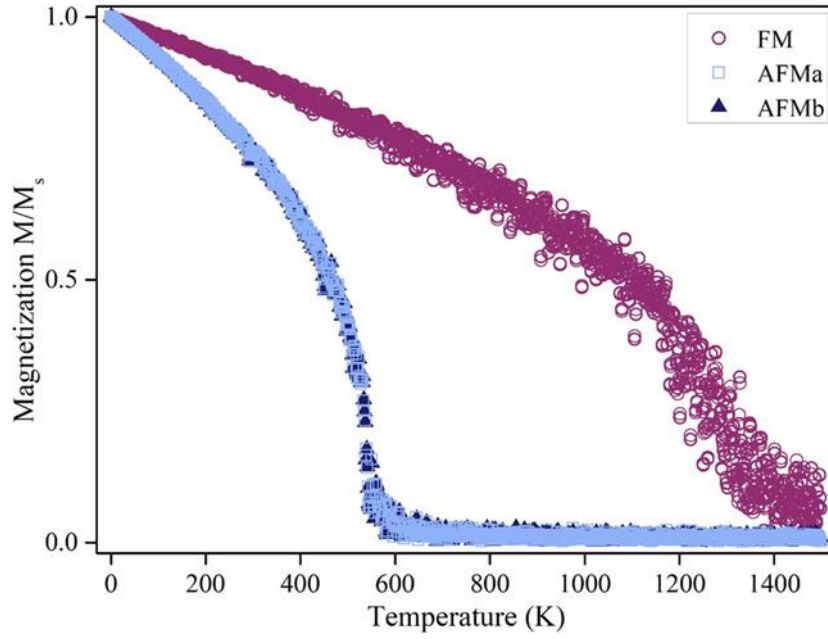


Figure S1: Curie (T_C) and Néel (T_N) temperatures of the FM and AFM respectively, obtained via simulations of the temperature dependence of the normalized magnetization (M/M_s) of each magnetic lattice and sublattice in the stack.

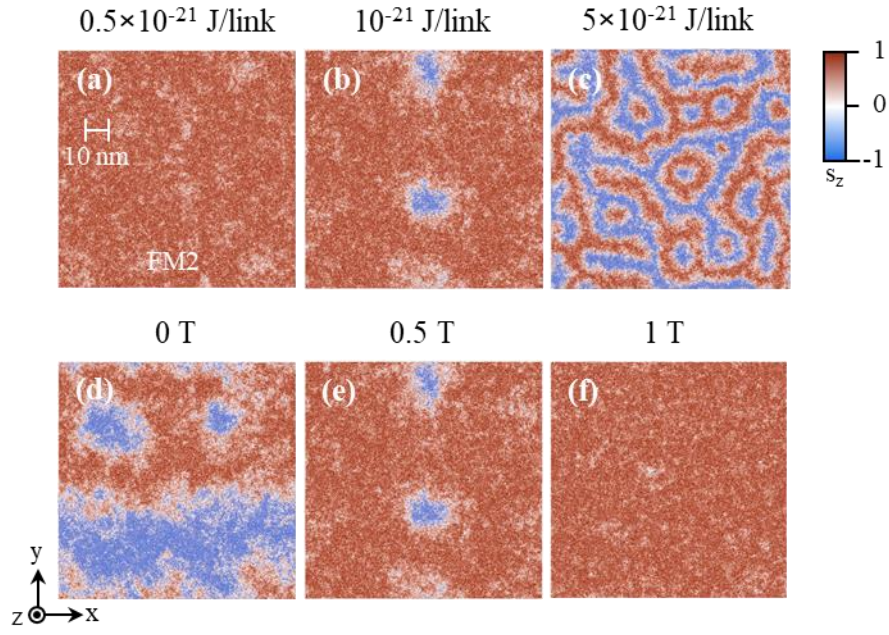


Figure S2: Top view cross section snapshots, at 600 K, of the evolution of the spin textures in the FM (2nd ML from the interface) under the effect of (a-c) the DMI parameter under an applied magnetic field of 0.5 T and (d-f) the strength of the applied magnetic field under a DMI parameter of 10⁻²¹ J/link. All other parameters are the same as in the main text, for the case of out-of-plane anisotropy.

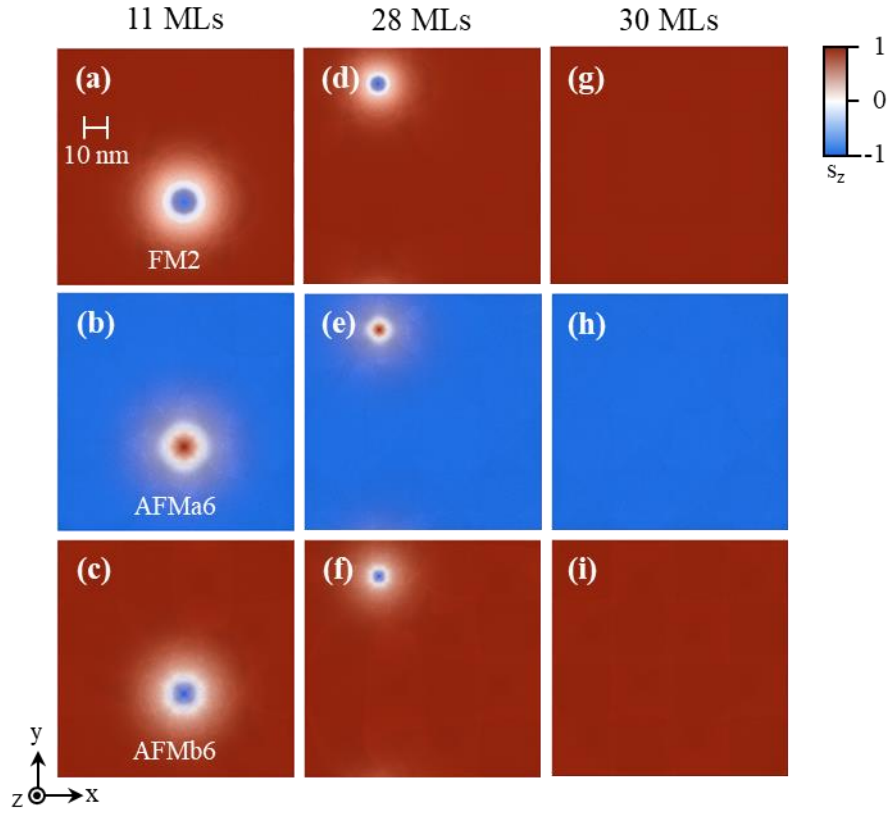


Figure S3: Top view cross section snapshots of the evolution of the final state of the Sk in the FM (first row, 2nd ML from the interface), and the AFM in the core (second row: AFMa, third row: AFMb, 6th ML from the interface) under the effect of the AFM thickness (11, 28, and 30 MLs).

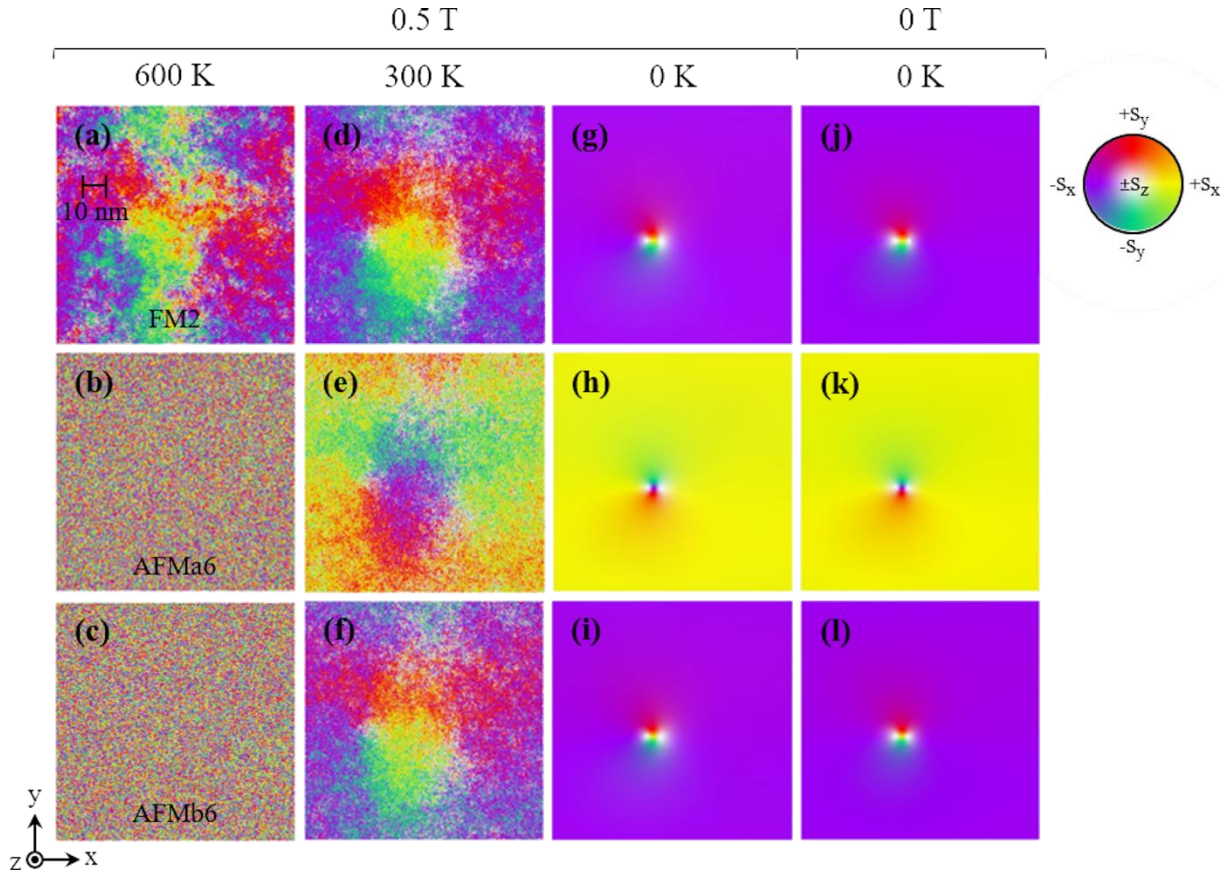


Figure S4: Top view cross section snapshots of the evolution of the in-plane components of the spin textures in the FM (first row, 2nd ML from the interface), and the AFM in the core (second row: AFMa, third row: AFMb, 6th ML from the interface): First column: field-induced nucleation in the FM, below T_C and above T_N . Second and third columns: imprinting and stabilization of the Bm in the AFM, via cooling across T_N . Fourth column: remanence state.

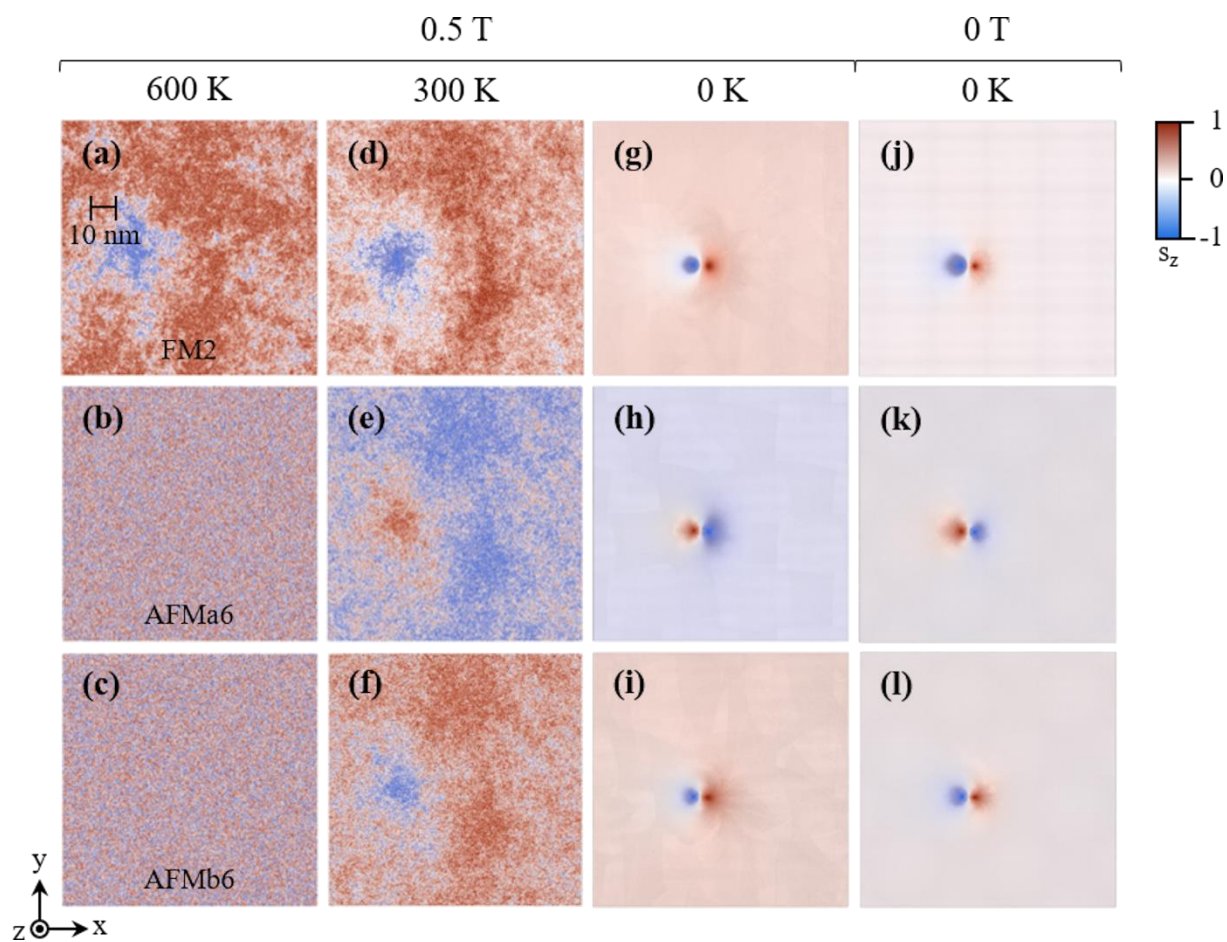


Figure S5: Same as Fig. S4 for the out-of-plane components.

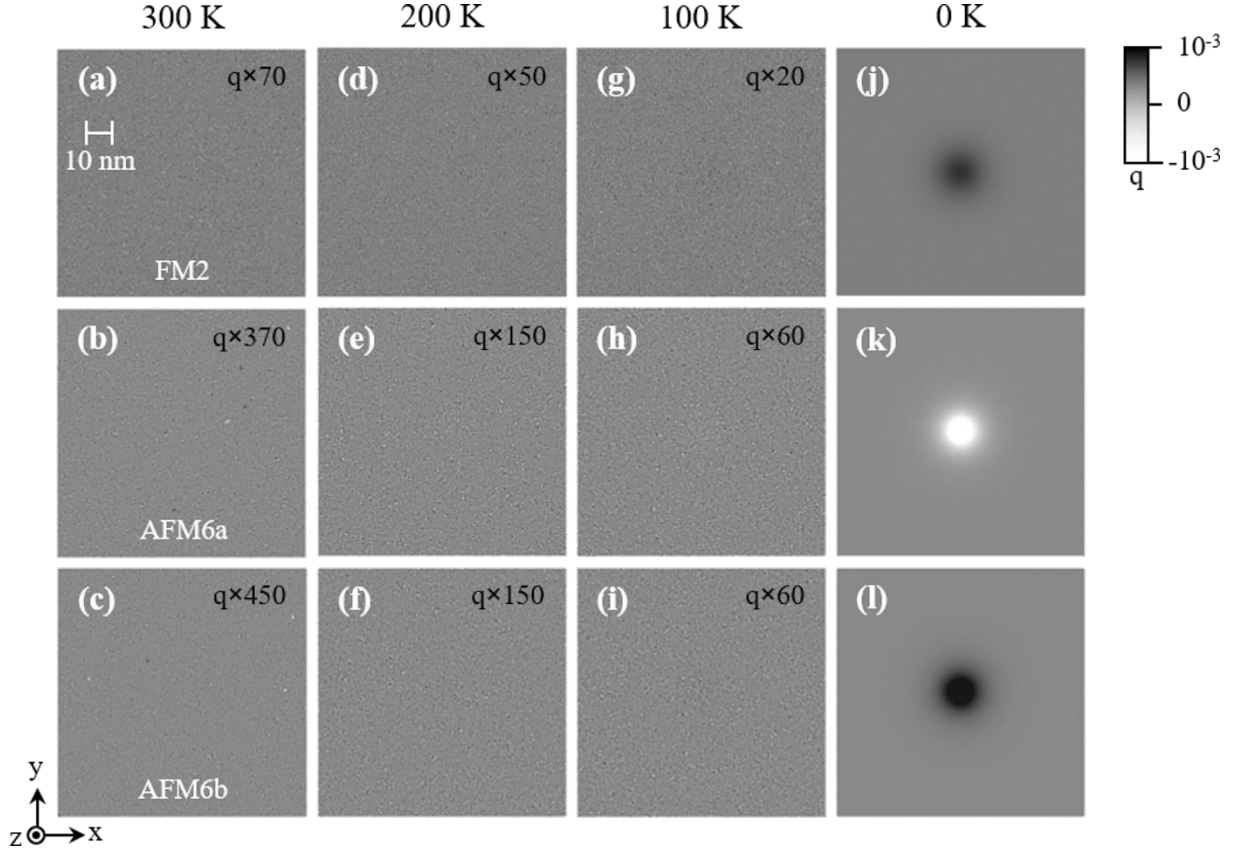


Figure S6: Spatial distribution of the topological charge density (q) in the FM (2nd ML from the interface) and the 11 MLs-thick AFM in the core (6th ML from the interface), for each sublattice: AFMa and AFMb, obtained from the raw data. Note that Q was calculated from these unprocessed q . To obtain Fig. 3(b-m) in the main text these raw data were post-processed with a Gaussian filter of the form:

$$\frac{\exp\left(-\frac{x^2+y^2}{2\sigma^2}\right)}{\sum_{(\Delta x, \Delta y) \in \left[-\frac{a(n-1)}{4}, \frac{a(n-1)}{4}\right]^2} \exp\left(-\frac{(x+\Delta x)^2+(y+\Delta y)^2}{2\sigma^2}\right)},$$
 with $a = 4.17 \text{ \AA}$, $n=17$ and $\sigma = \sqrt{20}$. This image post-processing makes the tiny spots in q visible.

Parameters	Simulation units	SI units	Simulation to SI units conversion formula
J_{FM}	13.3×10^{-21} J/link	6.38×10^{-11} J/m	$2/a$
J_{AFM}	-5.04×10^{-21} J/link	-1.71×10^{-11} J/m	$\sqrt{2}/a$
$J_{\text{FM-AFM}}$	10^{-21} J/link	4.80×10^{-12} J/m	$2/a$
$D_{\text{HM-FM}}$	10^{-21} J/link	2.30×10^{-2} J/m ²	$4/a^2$
$k_{\text{N,HM-FM}}$	2×10^{-24} J/atom	4.60×10^{-5} J/m ²	$4n_s/a^2$
$k_{\text{u,FM}} (Sk)$	10^{-24} J/atom	1.10×10^6 J/m ³	$8n_{\text{at}}/a^3$
$k_{\text{u,FM}} (Bm)$	-10^{-23} J/atom	-1.10×10^5 J/m ³	
$k_{\text{u,AFM}} (Sk)$	10^{-25} J/atom	1.10×10^5 J/m ³	
$k_{\text{u,AFM}} (Bm)$	-10^{-24} J/atom	-1.10×10^6 J/m ³	

Table S1: Conversion between simulation and SI units. We recall that the crystal structure is consistently set to that of two interpenetrating single cubic lattices and equivalent to rocksalt, with a lattice parameter $a = 4.17 \text{ \AA}$, corresponding to a unit cell size $a/2 = 4.17/2 \text{ \AA}$ and an equivalent number of atoms per unit cell $n_{\text{at}} = 1$ or per unit surface $n_s = 1$.